RESEARCH ARTICLE

ADVANCED FUNCTIONAL MATERIALS
www.afm-journal.de

Fabrication of Metal Nuclear Acid Framework to Enable Carrier-Free MNAzyme Self-Delivery for Gastric Cancer Treatment

Xiaodong Ma, Jiaqi Yan, Gongting Zhou, Yuanqiang Li, Meixin Ran, Chengcheng Li, Xiaodong Chen, Weijian Sun, Hongbo Zhang,* and Xian Shen**

Multi-component deoxyribozymes (MNAzymes) have shown extraordinary potential in precise gene therapy in vitro, however, the in vivo application is limited by complicated delivery systems. Herein, a novel DNA-metal binding mechanism is discovered, and metal-nucleic acid frameworks (MNFs) are built composed of MNAzymes and metal ions, which enable the carrier-free self-delivery of MNAzymes. Metal ions have a high affinity to DNA, however, the binding of metals with DNA at 20–30 base pair long (that normally a MNAzyme has) to form MNF structure is challenged by stringent high-temperature synthesis conditions, poor stability of the products, and lack of targeting capabilities. While, it is discovered that through folding and entanglement of the MNAzyme with an aptamer tail, and prolonging the sequence to 71 base pair, the metal MNAzymes binding is significantly improved and stabilized to MNF structure even at room temperature. Moreover, the aptamer tail also endows MNFs with targeting capabilities. As proof of concept, a carrier-free Ca/MNAzyme delivery system at room temperature, loaded with the model imaging protein BSA-Cy5 is synthesized. This system can effectively target Her-2 positive gastric cancer cells with the Her-2 responsive aptamer tail and initiate dual gene regulation, thereby inducing energy depletion in cancer cells.

1. Introduction

Following the confirmation of therapeutic DNAzymes' efficacy in human trials,[1] they have demonstrated significant potential in clinical medical applications.[2–4] However, a fundamental limitation of DNAzymes is their inability to distinguish between diseased and normal cells.[5,6] Consequently, during the treatment process, healthy cells can also internalize DNAzymes, leading to collateral damage.[7] Multicomponent deoxyribozyme (MNAzymes) represent an advanced structure derived from DNAzymes,[8] featuring a segmented catalytic core[9] and additional DNA recognition arms.[10] These arms endow MNAzymes with the capability to recognize biomarkers,[11,12] providing a switch mechanism and the ability to identify diseased tissues.[13,14] Despite over a decade of extensive exploration since their development, MNAzymes have been primarily explored for signal detection in biomarker response,[15–17] with scant reports in therapeutic applications.[18]

The catalytic activity of MNAzymes depends on metal cofactors,[19,20] and due to the poor permeability of cell membranes, MNAzymes face challenges in entering cells.[21,22] To address these challenges, the construction of MNAzyme delivery carriers is often complex, inevitably leading to the incorporation of non-therapeutic elements

---

X. Ma, X. Chen, W. Sun, X. Shen
Department of General Surgery
The First Affiliated Hospital of Wenzhou Medical University
Wenzhou, Zhejiang 325015, China
E-mail: fame198288@126.com; shenxian@wmu.edu.cn

X. Ma, X. Chen, H. Zhang, X. Shen
Joint Centre of Translational Medicine
Wenzhou Key Laboratory of Interdiscipline and Translational Medicine
The First Affiliated Hospital of Wenzhou Medical University
Wenzhou 325015, China
E-mail: hongbo.zhang@abo.fi

The ORCID identification number(s) for the author(s) of this article can be found under https://doi.org/10.1002/adfm.202406650

DOI: 10.1002/adfm.202406650

X. Ma, J. Yan, Y. Li, M. Ran, C. Li, H. Zhang
Pharmaceutical Sciences Laboratory
Faculty of Science and Engineering
Åbo Akademi University
Turku 20500, Finland

G. Zhou, W. Sun
Department of Gastrointestinal Surgery
The Second Affiliated Hospital and Yuying Children's Hospital of Wenzhou Medical University
Wenzhou, Zhejiang 325027, China

X. Chen, H. Zhang, X. Shen
Zhejiang Key Laboratory of Intelligent Cancer Biomarker Discovery and Translation
The First Affiliated Hospital of Wenzhou Medical University
Wenzhou 325015, China

H. Zhang
Turku Bioscience Centre
University of Turku and Åbo Akademi University
Turku 20500, Finland

into the carriers.[23–25] This not only burdens the body but also results in a low proportion of therapeutic MNAzymes within these carriers.[26–28] Furthermore, some tumor microenvironment-responsive carriers degrade prematurely before being absorbed by tumor cells,[29,30] releasing MNAzymes extracellularly and thus compromising treatment efficacy. These issues have slowed the research and development of MNAzymes.

Constructing MNAzymes and metal ion-based carrier-free nanomaterials could simplify DNAzyme delivery and overcome their inability to distinguish diseased cells. We define this novel structure of DNA-metal ion combinations as Metal-Nucleic Acid Frameworks (MNFs). However, DNA-metal binding faces many challenges. Specifically, DNA requires temperatures above 90 °C for three hours to form MNFs with metals like iron,[31,32] and 120 °C lasting for 3 days for metals like calcium[33] that less readily form MNF structures. These high-temperature synthesis conditions limit MNFs' use in delivering large molecular drugs, confining them to small molecule drugs and CpG oligonucleotides.[31,32] Moreover, MNFs produced using high-temperature methods lack targeting specificity and stability, degrading rapidly under physiological conditions, and impairing MNAzyme functionality in vivo. For example, the extensively studied Fe^{2+}/DNA MNFs completely degrade within two hours in PBS.[32] These issues impede the construction of carrier-free MNAzyme materials.

Prior research has primarily focused on the influence of nucleic acid bases and the concentrations of nucleic acids and metal ions on MNF construction. However, a significant aspect often overlooked is the impact of nucleic acid sequence length. Oligonucleotides, characterized by their lack of base stacking forces and adaptable spatial conformations, present a unique opportunity for exploration in MNF synthesis.[34] We hypothesize that increasing oligonucleotide sequence length theoretically enhances the folding probability during reaction. Folded DNA not only accommodates and coordinates more metal ions spatially but also concentrates the negative charge of DNA strands, attracting more positively charged metal ions.[35,36] This cumulative charge attraction significantly improves DNA-metal ion binding efficiency and stability, reducing the required temperature for MNF synthesis and enhancing product stability, enabling efficient room-temperature production and loading of large molecular active drugs. Cleverly, extending the length of DNA aids in the functional amplification of nucleotide sequences, aligning with the developmental needs of DNA nanotechnology in therapeutic applications. Integrating targeted nucleic aptamers with MNAzyme sequences into a new multifunctional MNAzyme sequence effectively resolves MNF nanoparticle targeting issues and the difficulty of free DNAzymes entering cells. This design mitigates the issue of pH-sensitive MNFs degrading in tumor microenvironments and releasing MNAzymes extracellularly,[37] improving the efficiency of cellular uptake, and enhances the synthetic efficiency and stability of MNFs.

In this study, we designed a miRNA-21-activated, calcium-dependent MNAzyme for cleaving Glucose transporter 1 (GLUT1) mRNA, integrating a human epidermal growth factor receptor-2 (Her-2) targeting aptamer[38,39] into the MNAzyme sequence to target Her-2 overexpressing cancer cells. This enabled room-temperature MNF synthesis with calcium ions and loading of model protein BSA-Cy5 for bioimaging. This design effectively enhanced MNFs' synthesis capability and targeted delivery to Her-2 overexpressing cells. It also differentiated healthy cells from cancer cells in the event of off-target effects, rendering DNAzyme-mediated GLUT1 mRNA silencing more selective, crucial for precision DNAzyme therapeutics. By specifically targeting GLUT1 in cancer cells, disruption of the pentose phosphate pathway (PPP) results, causing diminished cysteine synthesis and perturbation of GSH/ROS homeostasis,[40] effectively inducing DNA damage in cancer cells. Compared to small molecule inhibitors that suppress already produced GLUT1, MNAzymes can inhibit GLUT1 production from the onset, impeding cancer cell glucose uptake. Additionally, calcium ions, beyond activating the MNAzyme system, mediate mitochondrial apoptosis through calcium overload,[41–43] combined with GLUT1 silencing to enhance ATP depletion (**Scheme 1**).

In summary, our innovation lies in revealing the pivotal significance of DNA length in the interaction between DNA and metal ions. By employing DNA nanotechnology, we have intelligently designed a multifunctional MNAzyme sequence, enabling mild condition preparation of the carrier-free MNAzyme/Ca delivery system and efficient encapsulation of model proteins. Our work cleverly combines the strengths of DNAzymes and MNFs, overcoming the limitations of therapeutic DNAzymes while reducing MNFs″ synthesis conditions. These innovations significantly expand the medical applications of MNFs and DNAzymes.

2. Results

To construct a miRNA-21 responsive GLUT1 mRNA cleavage MNAzyme system, a selection was made between two established DNAzyme models, 17E and 10–23. Recent studies have delved deeper into the 17E DNAzyme's catalytic loop sequence and its affinity with various metal ions. For instance,[44] alterations in three base pairs within the catalytic center (N3-5, N9-11), and the replacement of thymine (T) with adenine (A) at position N12, have been shown to significantly increase the affinity of the 17E DNAzyme toward Ca^{2+} (**Figure 1a**). Additionally, under identical conditions of metal cofactor concentration, the catalytic activity of the 17E DNAzyme surpasses that of the 10–23 model.[45] Calcium, zinc, and magnesium ions are common cofactors for MNAzymes. Compared to zinc and magnesium, calcium ions play a unique role in cancer therapy due to their capability to induce calcium overload treatment. Additionally, compared to metals like iron and copper, which readily form MNFs with DNA structures, calcium ions exhibit weaker binding ability with DNA. Using calcium as an example better illustrates the influence of DNA sequence length on MNFs synthesis. Consequently, this study employs the 17E DNAzyme to develop an efficient, Ca^{2+}-responsive MNAzyme system for dual-gene regulation.

Following the identification of the catalytic center sequence and corresponding metal ions, miRNA-21 (abbreviated as T) was selected as the trigger gene. The trigger segment of the MNAzyme system was designed using a sequence complementary to miRNA-21, recognizing the elevated levels of miRNA-21 in many cancer cell lines compared to normal cells, marking it as a classic cancer biomarker.[46–48] The substrate recognition sequence was crafted to be complementary to GLUT1 mRNA (abbreviated as S). In terms of structure, the MNAzyme underwent segmentation from its catalytic center, resulting in two

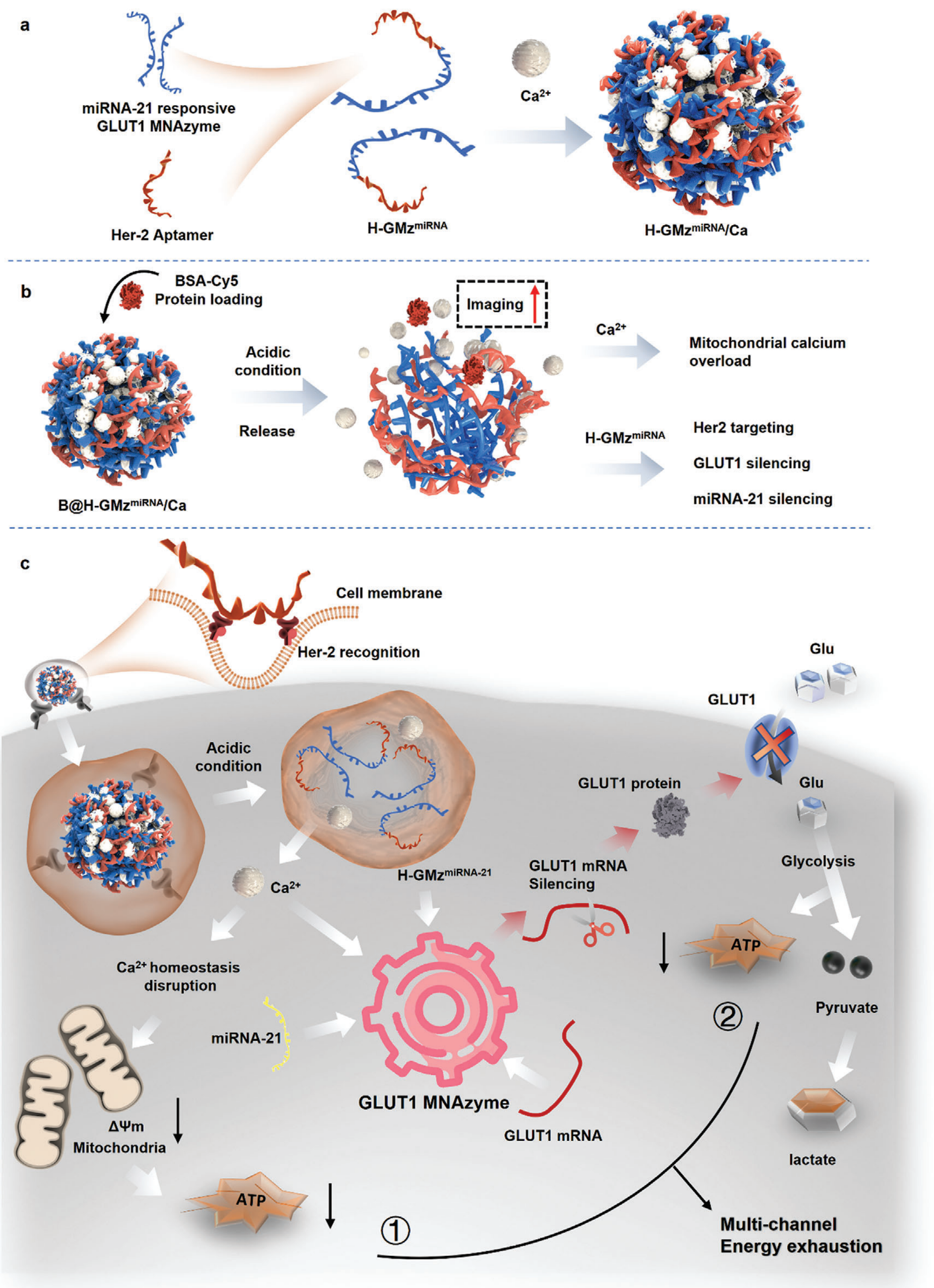

Scheme 1. Illustration depicting the preparation process of MNFs and their mediated energy exhaustion therapy mechanism. a) Preparation of MNFs. b) and c) Treatment mechanism of MNFs: After being taken up by gastric cancer cells, MNFs release MNAzyme and calcium ions under acidic pH conditions. MNAzyme self-assembles into active mode on-site by consuming miRNA-21 and Ca^{2+}, thereby silencing GLUT1 mRNA and inhibiting GLUT1. This not only affects the PPP pathway-mediated energy exhaustion therapy but also disrupts the homeostasis of GSH/ROS inside cancer cells, subsequently causing damage to the cell nucleus. In addition, silencing miRNA-21 leads to the upregulation of PTEN, accelerating cancer cell death. The excess Ca^{2+} produced by MNFs triggers mitochondrial calcium overload. Mitochondrial calcification reduces the production of adenosine triphosphate (ATP). Ultimately, dual-pathway control of ATP production achieves precise and efficient energy exhaustion therapy.

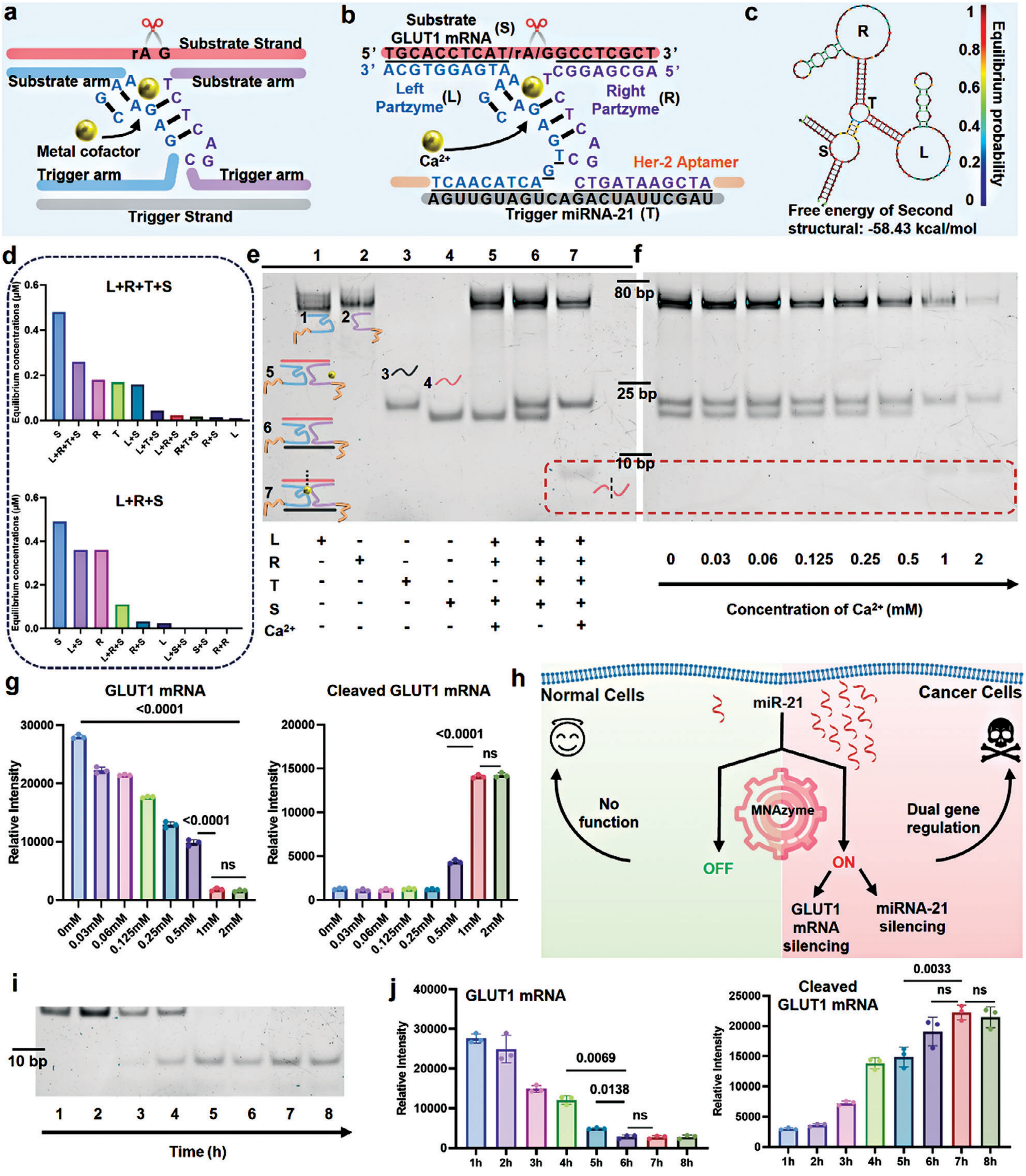

Figure 1. Construction and testing of the catalytic performance of calcium ion-dependent MNAzyme catalytic system responsive to miRNA-21, designed for the depletion of GLUT1 mRNA. a) General MNAzyme design structure based on 17E DNAzyme. b) Design scheme of a calcium ion-dependent MNAzyme system triggered by miRNA-21 for the cleavage of GLUT1 mRNA. c) Free energy of DNA complexes when T, R, L, and S are bound, as simulated by the NUPACK Web application. d) Equilibrium concentrations of L+R+T+S and L+R+S systems as simulated by the NUPACK Web application. e) Polyacrylamide gel electrophoresis experiments for different formulations of 20% polyacrylamide gel. f) Validation of the impact of Ca^{2+} concentration on the catalytic performance of the MNAzyme system. g) Quantification of the catalytic performance of the MNAzyme system under different calcium ion concentrations using ImageJ software. h) Construction logic of a cancer biomarker-responsive MNAzyme system. i) Validation of the effect of catalytic time on the performance of the MNAzyme system. j) Quantification of the catalytic performance of the MNAzyme system over different times using ImageJ software. (Experiments in E–J were independently repeated three times, with similar results. R is the right part enzyme, L is the left part enzyme, T is the trigger chain, and S is the substrate mRNA.).

distinct entities: a right-side Partzyme (denoted as R) and a left-side Partzyme (L), as depicted in Figure 1b. The system was further enhanced by attaching Her-2 targeting aptamer sequences to each Partzyme, creating a Ca^{2+}-responsive MNAzyme system capable of dual-gene regulation targeting Her-2 overexpressing cancer cells.

The NUPACK Web application[49] was employed for simulating the free interaction of four distinct DNA strands. The concentrations were set as L = 0.5 µm, R = 0.5 µm, T = 0.5 µm, and S = 1 µm. At the equilibrium state of the T+R+L+S configuration, this combination showcased the most stable secondary structure with the lowest free energy (-58.43 kcal mol^{-1}), as seen in Figure 1c and Figure S1 (Supporting Information), indicating superior stability over other combinations. In the L+R+S mixture (with concentrations of L, R, and S set to 0.5, 0.5, and 1 µm, respectively), a notable affinity was observed between S and L, resulting in the formation of a complex measured at 0.36 µm, while the binding efficiency between S and R (right partzyme) was significantly lower at only 0.031 µm (Figure 1d). These simulations suggest that MNAzyme assembly involves two steps: initial coupling of L and S, followed by binding of T or R (preferably T) with the L-S complex. Eventually, all four strands combine to form a stable MNAzyme configuration (Figure S2, Supporting Information).

After designing the MNAzyme sequence, its dual-gene regulatory functionality was assessed using 20% polyacrylamide gel electrophoresis (PAGE) (Figure 1e). Individual L (0.5 µm), R (0.5 µm), T (0.5 µm), and S (1 µm) strands displayed distinct bands in lanes 1, 2, 3, and 4, respectively. To test the MNAzyme system's discriminative ability between cancerous and healthy tissues, lane 5 explored its hydrolytic capacity on GLUT1 mRNA in the absence of miRNA-21 (including 1 mm Ca^{2+} and 1 µm S strand). Despite adequate Ca^{2+} levels, the MNAzyme failed to catalyze GLUT1 mRNA cleavage. In lane 6, due to insufficient metal ions, the S strand remained intact. However, with the addition of 1 mm Ca^{2+} and 0.5 µm miRNA-21 in lane 7, the substrate underwent cleavage, effectively vanishing and resulting in the emergence of two distinct new bands. These results indicated that the MNAzyme system, activated by miRNA-21, could reconnect Partzyme L and Partzyme R to reconstitute a complete catalytic core, restoring catalytic activity for Ca^{2+}-mediated multiple-turnover cleavage of GLUT1 mRNA and consuming miRNA-21 for dual-gene regulation.

Further verification of the impact of metal ion concentration on the MNAzyme system was conducted with a 6 h substrate catalytic hydrolysis test under varying Ca^{2+} levels (Figure 1f). L (0.5 µm), R (0.5 µm), T (0.5 µm), and S (1 µm) were added. The results showed a progressive decrease in S content as the Ca^{2+} concentration was progressively increased from 0 to 2 mm, there was a notable vanishing of the substrate band, and distinct cleavage bands of the S strand began appearing from 1 µm onward. These findings demonstrate that at 1 mm Ca^{2+} concentration, MNAzyme achieves optimal cleavage efficiency (Figure 1g). This verified that in gastric cancer cells overexpressing specific miRNA-21, this unique self-assembly of Partzyme into an MNAzyme, specifically geared for GLUT1 mRNA cleavage. This process led to the consumption of a significant amount of miRNA-21 within the cancer cells, thereby facilitating dual-gene regulation that simultaneously targets the disease-causing miRNA-21 and the therapeutic target gene GLUT1 (Figure 1h).

Finally, the influence of catalytic duration on the MNAzyme system was examined under conditions of L = 0.5 µm, R = 0.5 µm, T = 0.5 µm, S = 1 µm, and Ca^{2+} = 1 mm at 37 °C for varying periods (Figure 1i,j). As time progressed, a gradual reduction in the substrate was observed, with clear substrate cleavage bands appearing at 3 h and almost complete substrate depletion at 7 h. This confirmed the high efficiency of the MNAzyme in cleaving the substrate.

To explore whether sequences with multiple segments (longer in length) exhibit enhanced potential for MNF synthesis, we obtained three functional DNA fragments of different sizes: 20, 42, and 71 nucleotides from the company. These were mixed with 1 m $CaCl_2$ at equimolar concentrations to assess MNF generation efficiency. The shortest fragment, comprising 20 nucleotides, serves as the GLUT1 substrate strand. The 42-nucleotide fragment represents the Her-2 aptamer's sequence. A 71-nucleotide segment represents the partzyme sequence of the MNAzyme, extended with the Her-2 aptamer (**Figure** 2a). Findings indicate that the 71-nucleotide segment demonstrated a more effective binding with calcium ions, leading to a nanoparticle production rate ≈18% higher than the 42-nucleotide fragment. Surprisingly, the 20-nucleotide sequence was unable to bind with calcium ions to form nanoparticles (Figure S3, Supporting Information). These results provide clear macroscopic evidence that longer DNA sequences surpass shorter ones in terms of MNF synthesis efficiency.

Further analysis was conducted to understand the structural composition of MNFs, with a focus on the DNA and calcium content. For the H-GMz^{miRNA} sequence, with an initial DNA input of ≈44.87 µg, the actual DNA content was close to 40.97 µg, demonstrating a DNA utilization efficiency of 91.3%. In the case of the Her-2 aptamer's sequence, with an input of ≈46.86 µg, the DNA content in the product was also high at 88.2% efficiency, equating to ≈41.33 µg. The distinction, however, was in calcium ion utilization: the H-GMz^{miRNA} product contained 7.75 µg of calcium (calcium mass ratio of 15.9%), while the Her-2 aptamer's group had only 4.49 µg (calcium mass ratio of 9.8%). This suggested that while the DNA utilization efficiency remained consistent for both the Her-2 aptamer and H-GMz^{miRNA} sequence in MNF fabrication, longer DNA sequences demonstrated a greater affinity for calcium ions. Significantly, when the DNA sequence is reduced to 20 nucleotides, the resulting product, initially comprising ≈48.73 µg, becomes barely visible. Subsequent analysis revealed a mere 2.1 µg of DNA, representing only 4.3% efficiency, and a calcium content of 0.1 µg, corresponding to a calcium mass ratio of 4.5%. These observations highlighted the pivotal importance of DNA length in optimizing calcium ion binding.

The findings can be ascribed to the inherent characteristics of oligonucleotides, characterized by limited base stacking interactions and adaptable spatial structures. Thus, elongating the DNA sequences, rather than solely augmenting nucleotide concentration, has the capacity to enhance the folding and intertwining likelihood during reactions, thereby improving MNF synthesis efficiency and stability. Additionally, the intertwining of longer oligonucleotide chains aids in neutralizing the repulsion among DNA molecules, thereby enhancing the potential of intertwined

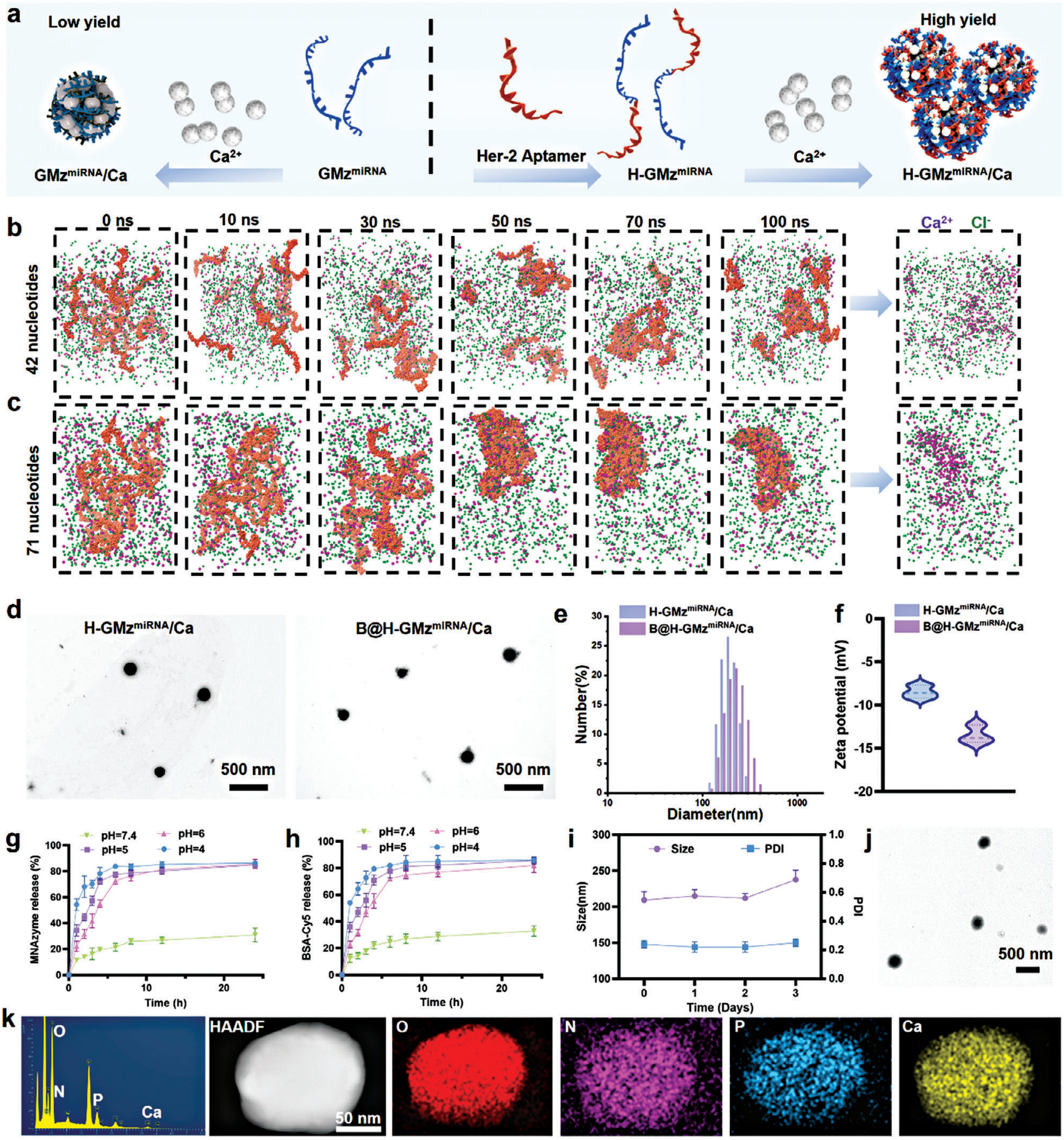

Figure 2. Analysis of the MNF synthesis mechanism based on the binding of long-chain DNA with calcium ions and characterization of MNF nanoparticles. a) The synthesis methodology of GMz$^{\text{miRNA}}$/Ca and H-GMz$^{\text{miRNA}}$/Ca MNFs. b,c) Computational modeling outcomes for DNA strands of different lengths, with identical nucleotide quantities and equivalent calcium ion concentrations. Calcium ions are visualized as purple orbs, and chloride ions are depicted as green orbs. The horizontal axis represents time, measured in nanoseconds (ns). d) TEM imagery of different MNF nanoparticle formations. e) Size and f) Zeta potential of different MNF NPs. g,h) The release of DNA and BSA from B@H-GMz$^{\text{miRNA}}$/Ca MNF NPs in different pH release media. i,j) Stability for MNF NPs in Milli-Q aqueous solution. K) EDS and elemental mapping assessments of MNF NPs.

DNA clusters to attract more calcium ions and ultimately leading to a higher MNF yield.

To verify this hypothesis, we established two systems with equivalent nucleotide counts in molecular dynamics simulation experiments (Figure 2b,c). System 1 comprised ten Her-2 aptamer sequences, whereas System 2 consisted of six H-GMz$^{\text{miRNA}}$ sequences. Throughout the 0–100 ns simulation, the shorter Her-2 aptamer sequences remained unstable and dispersed, showing little entanglement even at 100 ns. In contrast, H-GMz$^{\text{miRNA}}$ sequences entwined significantly, forming dense aggregations by

100 ns. This observation supports the idea that increased DNA length enhances the likelihood of entanglement.

Through integrating experimental observations with MD simulations, we confirmed the substantial influence of DNA length on MNF synthesis. By extending DNA length, we can enable the construction of calcium-based MNFs at ambient temperature, thereby expanding their scope for potential applications. Next, we delved into the DNA/Ca^{2+} concentration ratio's effect on nanoparticle size. We observed that a lower DNA: Ca^{2+} concentration (1:2) resulted in smaller nanoparticles ≈190 nm, while ratios of 1:1 and 2:1 produced sizes of ≈210 and 370 nm (Figure S4, Supporting Information), consistent with other studies. Significantly, with the augmentation in particle size, there was a corresponding decline in the electrostatic potential of the nanoparticles, indicating an elevated presence of negatively charged DNA within the larger particles (Figure S5, Supporting Information). Due to the group with a DNA/Ca^{2+} ratio of 1:2 exhibiting the smallest particle size, this ratio was chosen for MNF preparation in this study.

After confirming the influence of DNA length and the ratio of metal ions to DNA on the synthesis of MNFs, we examined the encapsulation efficiency of MNFs for proteins using BSA-Cy5 as a model protein. TEM results indicated that the morphology of B@H-GMz^{miRNA}/Ca NPs remained spherical without significant alterations after protein encapsulation (Figure 2d). Additionally, DLS measurements demonstrated a slight increase in the size of H-GMz^{miRNA}/Ca NPs after loading BSA, from ≈190 nm to ≈230 nm (Figure 2e), accompanied by a decrease in zeta potential (Figure 2f). Subsequently, we assessed the release behavior of DNA strands (Figure 2g) and BSA-Cy5 (Figure 2h) from B@H-GMz^{miRNA}/Ca nanoparticles under various pH conditions. The findings revealed that MNFs are pH-sensitive, with DNA sequences and BSA-Cy5 exhibiting similar release rates. In an acidic environment (pH 6), DNA and BSA-Cy5 were almost entirely released within 24 h, whereas in a neutral environment (pH 7.4), only ≈22% of the components were released in the same timeframe. These experimental observations demonstrate the refined pH responsiveness of the MNF nanosystem, highlighting its utility for precise and controlled therapeutic delivery.

Furthermore, to verify the stability of the products formed by the binding of long-chain DNA with Ca^{2+}, we conducted tests for 3 days. The results showed that MNFs formed by long-chain DNA and metals exhibited exceptional stability, with no significant changes in particle size or PDI in water (Figure 2i) or culture medium (Figure S6, Supporting Information). Observations of MNF morphology via TEM after 15 h showed that most MNF NPs retained their spherical shape, with a few exhibiting a decrease in volume. (Figure 2j). These results once again emphasize the advantages of using long-chain DNA to prepare MNFs, not only in terms of efficient room-temperature synthesis but also in the greatly enhanced stability of the MNF products. Finally, EDS analysis was conducted on H-GMz^{miRNA}/Ca NPs (Figure 1K). This analysis revealed the presence of essential elements within MNF, such as oxygen (O), nitrogen (N), phosphorus (P), and calcium (Ca), thus validating the successful synthesis of MNFs.

Following the effective establishment of the dual-gene regulatory MNAzyme system and the successful creation of the MNF delivery system, we proceeded to evaluate the targeting effectiveness of B@H-GMz^{miRNA}/Ca against Her-2 positive gastric cancer cells. Two distinct MNF formulations were designed: one containing the Her-2 aptamer sequence in the B@H-GMz^{miRNA}/Ca and the other with a mutated Her-2 aptamer sequence in B@MH-GMz^{miRNA}/Ca (keeping the total number of bases in both sequences constant). The cellular endocytosis capability of each group was reflected by monitoring the fluorescence intensity of BSA-Cy5 (represented in red). As depicted in **Figure 3a**, endocytosis was time-dependent, with the Her-2 aptamer-containing targeting group consistently exhibiting stronger fluorescence at each time point, indicating enhanced MNF uptake. Moreover, flow cytometry quantified the endocytosis results (Figure 3b), showing a trend consistent with confocal microscopy observations. The incorporation of the Her-2 aptamer facilitated the endocytosis of MNF NPs in the gastric cancer cell line, with the uptake efficiency of B@H-GMz^{miRNA}/Ca being ≈1.5 times higher than that of B@MH-GMz^{miRNA}/Ca (Figure 3c). Additionally, we utilized NCI-N87 cells to construct a spheroid model to verify the penetrative capability of B@H-GMz^{miRNA}/Ca MNFs within tumor tissues. Intriguingly, groups containing the Her-2 aptamer demonstrated stronger tumor penetration capabilities within the same duration compared to those without the Her-2 aptamer. The B@MH-GMz^{miRNA}/Ca group remained on the surface of the tumor spheroid at 10 h (Figure S7, Supporting Information), whereas B@H-GMz^{miRNA}/Ca had already penetrated into the interior of the tumor spheroid (Figure S8, Supporting Information). Subsequently, to assess the universality of B@H-GMz^{miRNA}/Ca MNF's targeting of Her-2 overexpressing cancer cells, we also conducted tests in SNU-216 gastric cancer cells. The experimental outcomes were similar to those with the N87 cell line (Figure S9, Supporting Information), where the Her-2 aptamer also enhanced the uptake of MNF by this cell line.

To verify the Her-2 aptamer's effect on the cellular uptake of free MNAzymes, we tested using Cy5-labeled DNA sequences, H-GMz^{miRNA}-Cy5 and MH-GMz^{miRNA}-Cy5. As shown in Figure 3d, the uptake efficiency of H-GMz^{miRNA}-Cy5 was six times higher than that of MH-GMz^{miRNA}-Cy5. In contrast, in the NHDF healthy cell line, the uptake of B@H-GMz^{miRNA}/Ca and B@MH-GMz^{miRNA}/Ca was compared. The experiment involved assessing cellular uptake at 2, 4, and 6 h time points using confocal microscopy and flow cytometry to measure the fluorescence intensity, indicating nanoparticle ingestion (Figures S10 and S11, Supporting Information). This comparison revealed no significant differences in uptake, likely attributed to the absence of Her-2 expression in normal cells. Consequently, the Her-2 aptamer-modified MNF did not enhance nanoparticle ingestion in healthy NHDF cells. Based on these experiments, we found that the H-GMz^{miRNA} showed dual targeting capabilities on NCI-N87 cells: both in terms of the MNF NPs and the free MNAzymes (Figure 3e).

Lysosomal escape results (Figure 3f) indicated that the fluorescence overlap between MNF nanoparticles (red signal) and lysosomes (green signal) decreased after 6 h, with the Pearson Correlation Coefficient (PCC) number dropping from 0.76 to 0.53. By comparing fluorescence curves at two time points, we observed almost identical trends at 3 h, but a significant decrease in overlap at 6 h (Figure 3g), confirming the effective escape of MNF NPs from lysosomes.

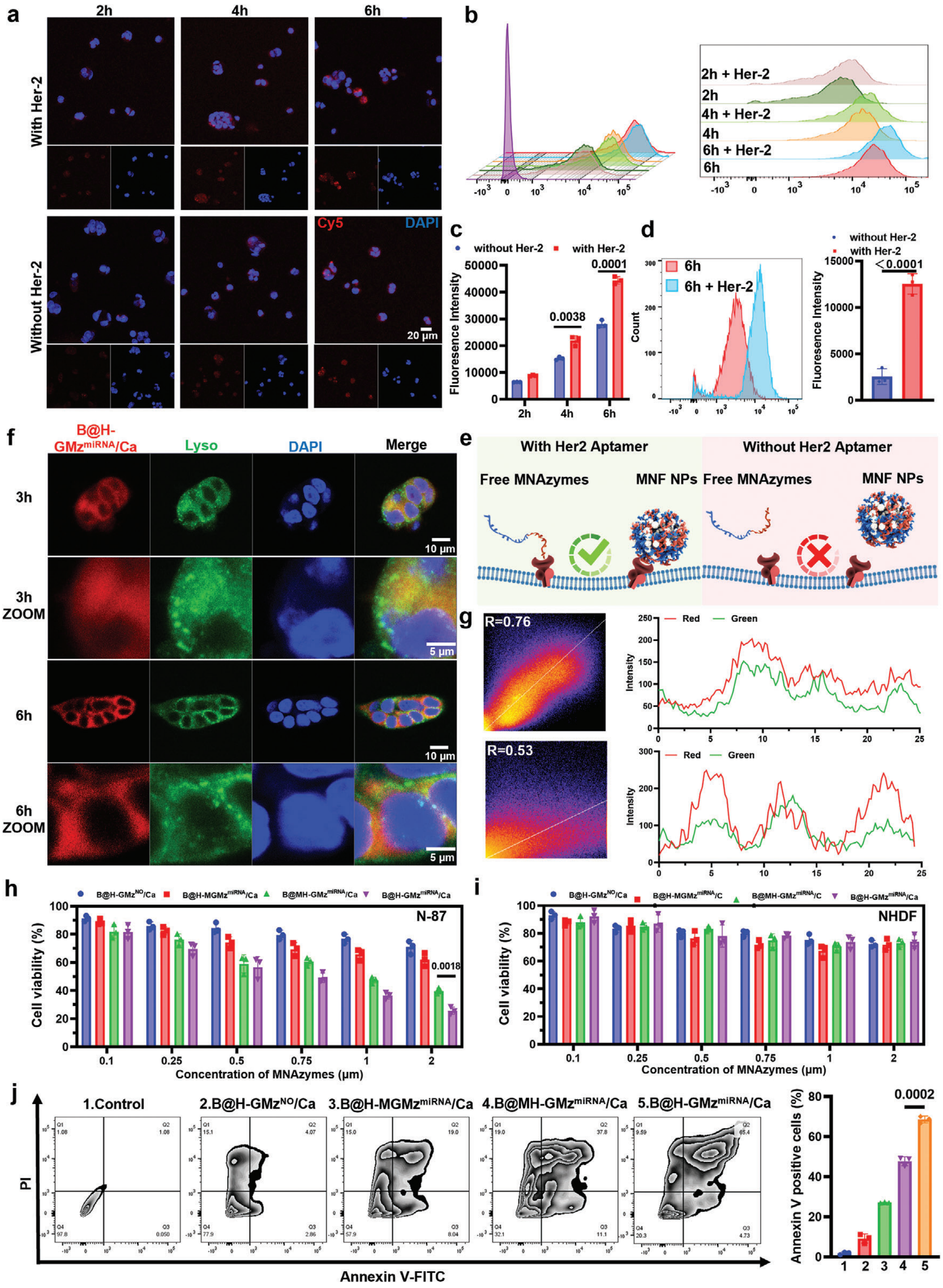

Figure 3. Validation of the targeting ability and cytotoxicity of each material. a) Evaluation of the targeting ability of various materials on N87 cells using fluorescence confocal microscopy. b) Images obtained from flow cytometry analysis to assess the cellular uptake of different materials. c) Statistical chart of flow cytometry results. d) Images obtained from flow cytometry analysis to assess the cellular uptake of different free DNA. e) Schematic representation of the targeting mechanism of Her-2 modified materials. f) Assessment of the lysosome escape capability of MNF materials after entering N87 cells using fluorescence confocal microscopy. g) Analysis of lysosome escapes results using ImageJ software. h) Cytotoxicity experiments of different material groups on N87 cells. i) Cytotoxicity experiments of different material groups on NHDF cells. j) Analysis of cell apoptosis in N87 cells treated with different materials using Annexin V-FITC/PI staining.

Having confirmed the efficient delivery of therapeutic agents to the cytoplasm, we set up four nanoformulation groups to preliminarily study their toxicity on N87 gastric cancer cells and normal human dermal fibroblast NHDF cells, using WST-1 and apoptosis assays. The groups were B@H-GMz^{NO}/Ca with a mutated miRNA recognition sequence, B@H-MGMz^{miRNA}/Ca with a mutated GLUT1 substrate sequence, B@MH-GMz^{miRNA}/Ca with a mutated aptamer sequence, and the final formulation B@H-GMz^{miRNA}/Ca. Results in Figure 3h showed that despite NP concentrations reaching 2 μm, cell viability remained high, approximately close to 75% and 68% for the B@H-GMz^{NO}/Ca and B@H-MGMz^{miRNA}/Ca groups, respectively, as they lacked the complete MNAzyme catalytic system. However, the group with only the Her-2 aptamer mutated, B@MH-GMz^{miRNA}/Ca, showed a reduction in cell viability to ≈39%. The final formulation, B@H-GMz^{miRNA}/Ca, had the highest inhibitory effect on gastric cancer cells, reducing cell viability to ≈26%, highlighting the importance of Her-2 aptamer modification. Similar conclusions were also obtained from the SNU-216 cell lines (Figure S12, Supporting Information). Despite high concentrations, these four MNF formulations showed no significant cytotoxicity in healthy cell lines (Figure 3i), likely due to the lower release of MNAzymes and calcium ions in the microenvironment of healthy cells, and the absence of miRNA21 to initiate MNAzyme cleavage. These results indicate that the MNAzyme system has excellent selectivity, effectively distinguish between cancer and healthy cells, achieving precise MNAzyme therapy. From apoptosis assay results (Figure 3j), ≈10% of cells began apoptosis in the B@H-GMz^{NO}/Ca group after 24 h of treatment, while ≈27.0% of cells entered apoptosis in the B@H-MGMz^{miRNA}/Ca group. This preliminary result suggests that miRNA silencing can induce apoptosis. Furthermore, ≈47% of cells underwent apoptosis in the B@MH-GMz^{miRNA}/Ca formulation group. Finally, for the final formulation B@H-GMz^{miRNA}/Ca, ≈68% of the cells entered late apoptosis, attributable to enhanced cell uptake by the aptamer, GLUT1 silencing, PTEN regulation, and calcium overload synergistically.

Subsequent to initially confirming the toxicity of the MNF formulation on gastric cancer and healthy cells, we delved deeper into the dual-gene regulatory effects of MNF after its entry into cancer cells. Initially, we assessed the changes in intracellular Ca^{2+} concentrations post MNF introduction. Using Fluo-4 AM for green fluorescence visualization of intracellular calcium, observations were made through CLSM (**Figure** 4a), with relative Ca^{2+} intensities further quantified using ImageJ. As anticipated from MNF in vitro release simulations in the acidic microenvironment of gastric cancer, all MNF formulations markedly elevated intracellular calcium levels. Interestingly, groups containing the Her-2 targeting aptamer exhibited ≈37% higher calcium fluorescence intensity compared to groups without the aptamer, corroborating the significant role of Her-2 targeting in elevating intracellular calcium concentration. High intracellular calcium not only provides the necessary cofactor for the MNAzyme system but also contributes to inducing mitochondrial Ca^{2+} overload.

To visually confirm whether the MNAzyme could identify and capture intracellular miRNA-21, the fluorescence in situ hybridization (FISH) method was used to observe free miRNA-21 within cells (Figure 4b; Figure S13, Supporting Information). This method tagged endogenous miRNA-21 with green fluorescence. The results demonstrated that the control group exhibited stronger green fluorescence, while upon the addition of B@H-GMz^{NO}/Ca, there was no decrease in fluorescence intensity. However, upon adding B@H-MGMz^{miRNA}/Ca, B@MH-GMz^{miRNA}/Ca, and B@H-GMz^{miRNA}/Ca, varying degrees of decrease in miRNA fluorescence were observed, with B@H-GMz^{miRNA}/Ca showing the most significant reduction, ≈88%. These outcomes suggest that MNAzyme can effectively capture miRNA-21 in cancer cells, ensuring the formation of the MNAzyme catalytic system.

Subsequently, to investigate whether MNAzyme could effectively cleave GLUT1 mRNA, leading to downregulation of GLUT1 protein in N87 cells, Cy3-labeled secondary antibodies were used (Figure 4c). These antibodies marked the GLUT1 protein with red fluorescence. We observed that the control group displayed stronger red fluorescence, with negligible differences in fluorescence intensity upon adding B@H-GMz^{NO}/Ca and B@H-MGMz^{miRNA}/Ca. Upon adding B@MH-GMz^{miRNA}/Ca and B@H-GMz^{miRNA}/Ca, a noticeable decrease in GLUT1 protein fluorescence was observed, with B@H-GMz^{miRNA}/Ca showing the most marked reduction, ≈91%. These preliminary results suggest that MNAzyme can cleave GLUT1 mRNA within cells, reducing GLUT1 protein expression.

Following this, Western blot experiments were conducted to accurately verify protein expression in cells, with GLUT1/β-actin and PTEN/ β-actin ratios calculated using ImageJ (Figure 4d). In the N87 cell line, we found that B@MH-GMz^{miRNA}/Ca and B@H-GMz^{miRNA}/Ca significantly downregulated GLUT1 expression (≈38% and 17%, respectively), indicating that the MNAzyme system in its active state can effectively cleave GLUT1 mRNA, reducing GLUT1 protein. In contrast, B@H-GMz^{NO}/Ca and B@H-MGMz^{miRNA}/Ca groups showed no notable change in GLUT1 protein content compared to the control, consistent with CLSM results. The abnormal loss of miRNA led to an increase in PTEN protein expression, with B@H-MGMz^{miRNA}/Ca, B@MH-GMz^{miRNA}/Ca, and B@H-GMz^{miRNA}/Ca groups showing varying degrees of upregulation in PTEN protein. In the NHDF healthy cell line (Figure S14, Supporting Information), we found that none of the formulations could downregulate GLUT1 expression. These results demonstrate that the MNAzyme system possesses excellent recognition capabilities, effectively performing dual-gene regulation in cancer cells while remaining inactive in healthy cells.

The inhibition of GLUT1 not only works in conjunction with mitochondrial calcification to enhance energy depletion in cancer cells but also disrupts the GSH synthesis pathway, thereby triggering the breakdown of the GSH/ROS balance within cancer cells (Figure 4e). Therefore, we utilized assay kits to test the relative quantities of key substances in different pathways of N87 cells treated with various MNF formulations. For groups that effectively exerted GLUT1 inhibitory functions, both B@MH-GMz^{miRNA}/Ca and B@H-GMz^{miRNA}/Ca groups observed a decrease in the relative quantities of 6-Phosphogluconate, Cysteine, ATP, and GSH, while other groups did not show significant changes compared to the control group (Figure 4f). These outcomes highlight the dual effects produced by the inhibition of GLUT1.

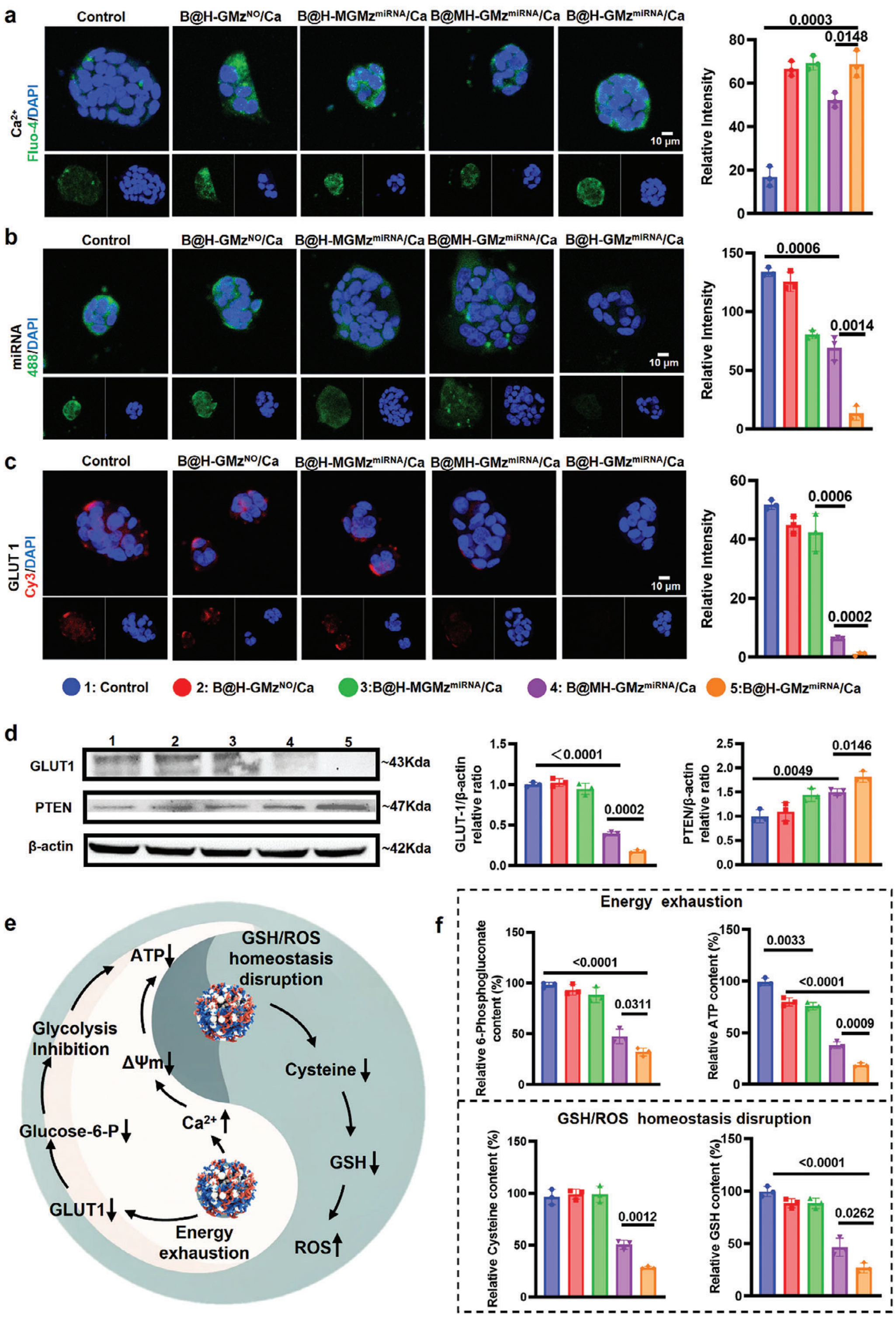

Figure 4. Analysis of Dual Genes Modulation and Calcium Overload. a) Visualization of Ca^{2+} concentration levels utilizing Fluo-4 AM as the marker dye. b) The levels of intracellular miRNA-21 were quantified using the fluorescence in situ hybridization (FISH) technique. c) Fluorescence confocal microscopy was used to assess the impact of various groups on the GLUT1 gene within cells. GLUT1 protein inside cells was identified with an antibody, emitting red fluorescence, while cell nuclei were marked with DAPI, appearing in blue. d) The levels of GLUT1 and PTEN proteins were analyzed through western blot analysis. The final concentrations for each experimental group were set at 2 μM for each partzyme. e) Schematic representation of the selective Ca^{2+} overload and GLUT1 inhibition for the suppression of tumor energy metabolism and disruption of ROS/GSH homeostasis. f) Characterization of intracellular PPP metabolism, 6-Phosphogluconate, and Cysteine consumption processes, as well as GSH and ATP synthesis in N87 cells.

Upon validating the specific bi-functional gene regulation efficiency of the MNAzyme system incorporating the Her-2 aptamer (designated B@H-GMz^{miRNA}/Ca) in targeting gastric cancer cells, our focus expanded to encompass the examination of various cellular damages post the dual-gene modulation. This included DNA damage, mitochondrial injuries from calcium excess, and disruptions in ROS/GSH equilibrium due to GLUT1 suppression (**Figure** 5a). The investigative study spanned five distinct groups: Control group, B@H-GMz^{NO}/Ca, B@H-MGMz^{miRNA}/Ca, B@MH-GMz^{miRNA}/Ca, and B@H-GMz^{miRNA}/Ca.

The decline in mitochondrial membrane potential (ΔΨm), a marker of early apoptosis, was gauged using the JC-1 dye, with the relative intensities quantified through ImageJ. Elevated ΔΨm results in JC-1 forming aggregates emitting red fluorescence, whereas lowered potential leads to monomeric JC-1 emitting green fluorescence. Illustrated in Figure 5b, each of the four treatment groups showed a decrease in red fluorescence compared to the control, indicating that the MNF's abundant calcium ions induced calcium overload in cancer cells, thus reducing membrane potential. Particularly, the B@MH-GMz^{miRNA}/Ca and B@H-GMz^{miRNA}/Ca groups evidenced a marked decrease in red fluorescence, with red-to-green fluorescence ratios significantly reduced to 21% and 13%, respectively. This reduction is likely a result of GLUT1 inhibition disturbing ROS/GSH balance, further aggravating mitochondrial damage, augmented by the presence of the Her-2 aptamer.

The mitochondrial permeability transition pore (MPTP), another critical mitochondrial status marker, was also evaluated (Figure 5c). Post mitochondrial damage, an increase in MPTP opening was observed. The mitochondrial Calcein fluorescence intensity in the B@H-GMz^{NO}/Ca, B@H-MGMz^{miRNA}/Ca, and B@MH-GMz^{miRNA}/Ca groups is by ≈56%, 35%, and 18%, respectively, highlighting a significant elevation in mitochondrial permeability. In the B@H-GMz^{miRNA}/Ca group, the decrease in Calcein fluorescence was even more pronounced at 4%, a clear indication of a substantial increase in mitochondrial membrane permeability. These outcomes are in sync with the findings from the mitochondrial membrane potential tests.

Next, bio-TEM analysis was employed to visually examine mitochondrial morphology across the studied groups (Figure 5d). The control group's mitochondria maintained normal morphology with distinct cristae and intact structures. Contrastingly, in the groups treated with the MNF formulations, notable mitochondrial damage was observed, characterized by membrane disruptions. The B@H-GMz^{NO}/Ca and B@H-MGMz^{miRNA}/Ca groups exhibited less severe and fewer mitochondrial cavities, while significant mitochondrial damage was evident in the B@MH-GMz^{miRNA}/Ca group. Most notably, the B@H-GMz^{miRNA}/Ca group displayed extensive mitochondrial damage with numerous hollow cavities, underscoring the combined impact of calcium overload, GLUT1 inhibition, and the incorporation of the Her-2 aptamer.

To ascertain if inhibiting GLUT1 expression significantly elevated intracellular ROS levels, ROS was marked with green fluorescence (Figure 5e). In the B@H-GMz^{NO}/Ca and B@H-MGMz^{miRNA}/Ca groups, there was little to no change in ROS fluorescence. However, in the B@MH-GMz^{miRNA}/Ca and B@H-GMz^{miRNA}/Ca groups, there was a significant increase in ROS levels, with the latter showing an ≈46% enhancement in fluorescence intensity compared to the former. These results provide compelling evidence of the MNAzyme system's capability to effectively elevate intracellular ROS levels.

Finally, immunofluorescence experiments with a green fluorescent antibody against γ-H2AX assessed the level of DNA damage (Figure 5f). The B@H-GMz^{NO}/Ca and B@H-MGMz^{miRNA}/Ca formulations induced no significant nuclear damage. For the effective treatment groups, B@MH-GMz^{miRNA}/Ca and B@H-GMz^{miRNA}/Ca, the latter showed ≈31% increase in γ-H2AX fluorescence intensity, indicating an enhanced DNA damaging efficacy due to GLUT1 inhibition. In the B@H-GMz^{miRNA}/Ca group, nuclear damage was also observable in bio-TEM images (Figure S15, Supporting Information). These findings, taken together, indicate the significant impact of the B@H-GMz^{miRNA}/Ca MNF in triggering ROS-induced DNA damage, thus demonstrating its efficacy in cancer cell modulation.

Motivated by the significant inhibitory potency and biocompatibility demonstrated in vitro, we extended our study to the nanosystems' performance in a live setting. All animal procedures mentioned in our study were conducted strictly in accordance with the Guidelines for the Care and Use of Laboratory Animals. Approval was granted by the Institutional Animal Care and Use Committee (IACUC) of Zhejiang Center of Laboratory Animals (ZJCLA), reference number ZJCLA-IACUC-20020188. Luciferase/GFP-labeled gastric cancer cells were used to surgically construct an in situ gastric cancer tumor model. The average radiance of luciferin bioluminescence was employed to indicate the progression of in situ tumor growth and for ex vivo visualization of the tumor. We initiated in vivo imaging to track the distribution of NPs following intravenous introduction, as depicted in **Figure** 6a. Interestingly, MNF NPs crafted with an altered Her-2 sequence (B@MH-GMz^{miRNA}/Ca) predominantly gathered in the kidneys due to the natural capture of negatively charged nanostructures by renal pathways. Contrarily, B@H-GMz^{miRNA}/Ca showed marked tumor localization in the stomach, maintaining strong fluorescence signals up to 24 h post-injection, emphasizing the essential function of the Her-2 aptamer in directing MNF materials to cancer cells.

Subsequent to in vivo imaging, ex vivo analyses at the 24 h point were conducted to study nanodevice fluorescence across different organs (Figure 6b). Both MNF variations primarily accumulated in the kidneys, liver and tumor, with B@MH-GMz^{miRNA}/Ca showing the highest kidney retention. However, kidney retention for B@H-GMz^{miRNA}/Ca NPs was about half that of the B@MH-GMz^{miRNA}/Ca variant. Additionally, the tumor area's fluorescence for B@H-GMz^{miRNA}/Ca was significantly higher than B@MH-GMz^{miRNA}/Ca, underscoring the Her-2 sequence's contribution to tumor-targeting. To evaluate therapeutic effects, in vivo tumor studies were executed, monitoring tumor growth using luciferin bioluminiscence (Figure 6c). Tumor sizes in the control, B@H-GMz^{NO}/Ca and B@H-MGMz^{miRNA}/Ca groups enlarged over time (Figure 6e,f), while B@MH-GMz^{miRNA}/Ca and B@H-GMz^{miRNA}/Ca significantly reduced tumor sizes, with the latter nearly eradicating the tumor by day 21 (Figure 6g), showcasing a synergistic impact of GLUT1 inhibition and calcium homeostasis disruption. The safety profiles of the groups were thoroughly investigated. Mice body weights

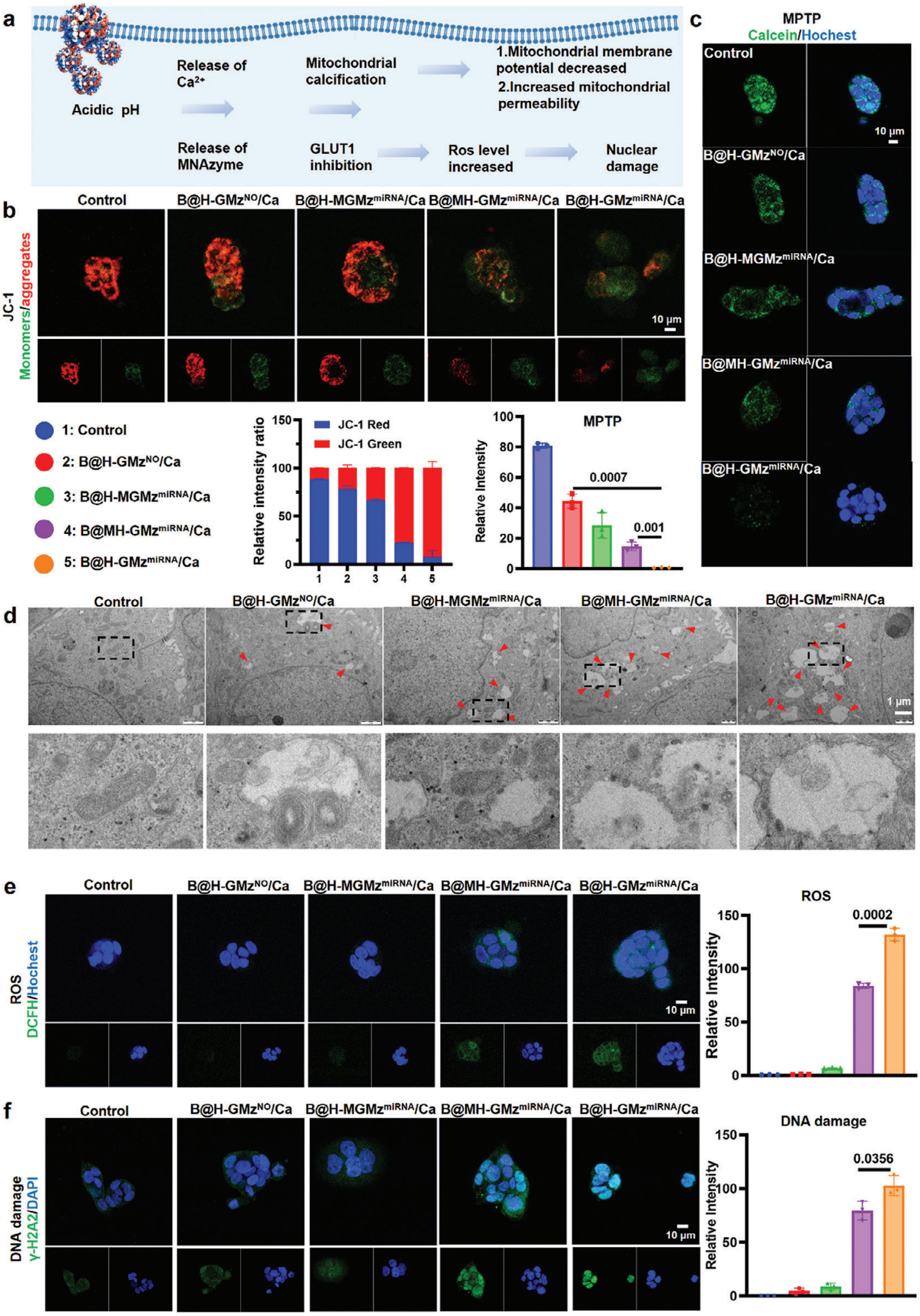

Figure 5. Analysis of Combined Therapeutic Effects Dual Genes Modulation and Calcium Overload. a) Mechanism of Nucleus and Mitochondrial Damage. b) Evaluation of mitochondrial membrane potential. In cells with intact and functioning mitochondria, JC-1 dye aggregates emitted red fluorescence, while in cells with diminished mitochondrial membrane potential, JC-1 in its monomeric state produced green fluorescence. c) Utilization of a combined marker of Calcein AM and $CoCl_2$ for determining mitochondrial membrane permeability. In scenarios with intact MPTP, $CoCl_2$ suppressed cytoplasmic Calcein fluorescence, highlighting mitochondrial green fluorescence. d) Bio-TEM photographs depicting mitochondria under different cellular states. e) Determination of intracellular levels of reactive oxygen species (ROS) using the green fluorescent marker 2′,7′-Dichlorodihydrofluorescein diacetate (DCFH-DA). f) Examination of nuclear DNA damage.

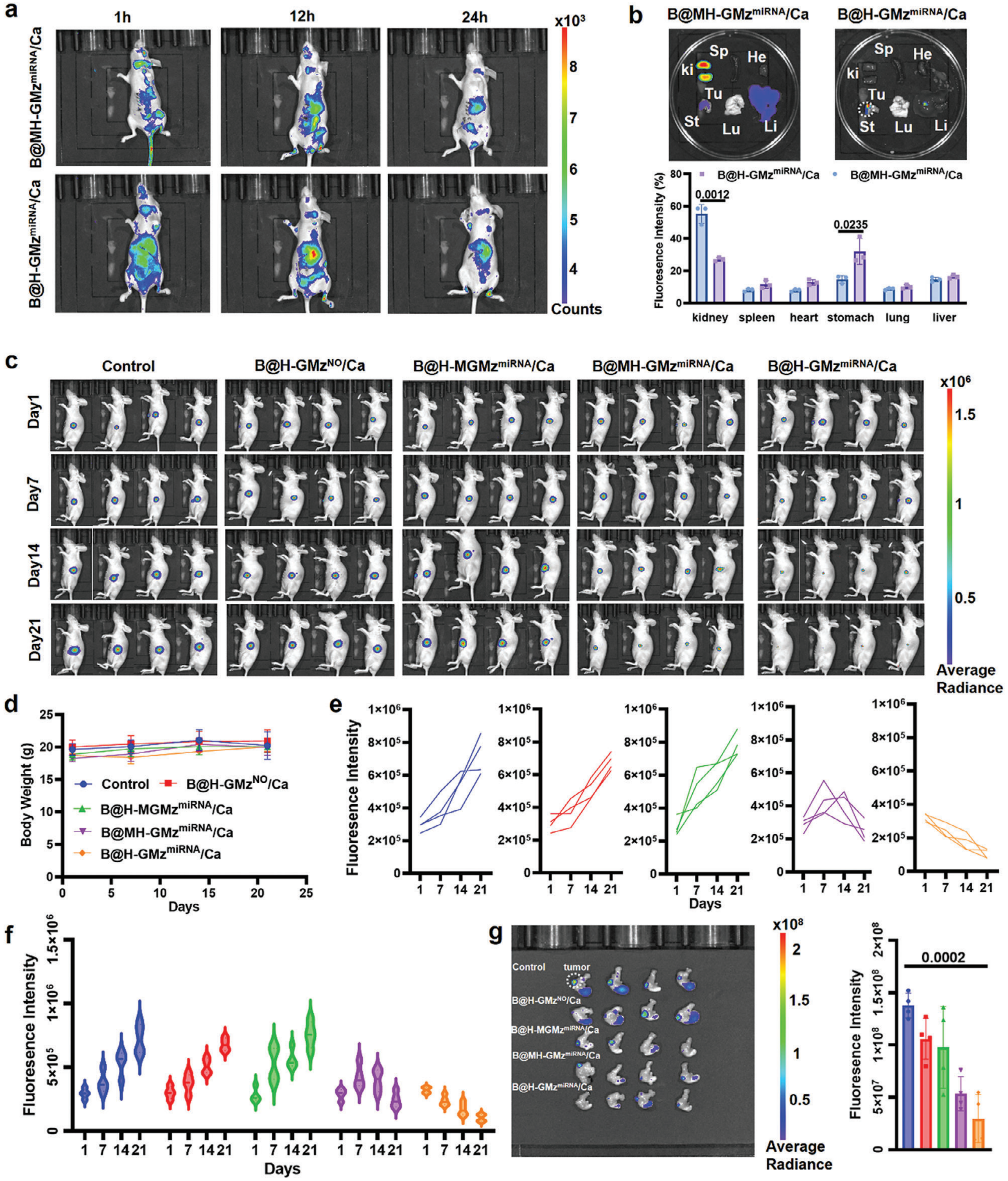

Figure 6. Analysis of Nanomaterial Distribution and Therapeutic Impact in Murine Models. The study aims to evaluate the regulatory effects of dual genes and the efficacy of calcium overload., featuring five distinct groups: Control, B@H-MGMz^{miRNA}/Ca, B@MH-GMz^{miRNA}/Ca, B@H-GMz^{NO}/Ca, and B@H-GMz^{miRNA}/Ca. a) Intravenous injection of MNF NPs and their subsequent distribution within the mice. b) Visualization of these nanomaterials in dissected organs, encompassing heart, liver, spleen, lungs, kidneys, and stomach. c) An in vivo examination of tumor suppression in murine subjects. d) Fluctuations in body weight over the course of treatment. e) Observation of time-dependent alterations in fluorescence intensity at the tumor sites in individual mice. f) Violin plots depicting the group-wise mean shifts in fluorescence intensity at the tumor locations. g) EGF-based fluorescence imaging and measurement of gastric tumors in the mice. Due to inherent fluorescence from the adjacent gastric substances, analyses were meticulously concentrated on the demarcated tumor areas. The unit of bioluminescence imaging in (c–g) is [p s^{-1} cm^{-2} sr^{-1}].

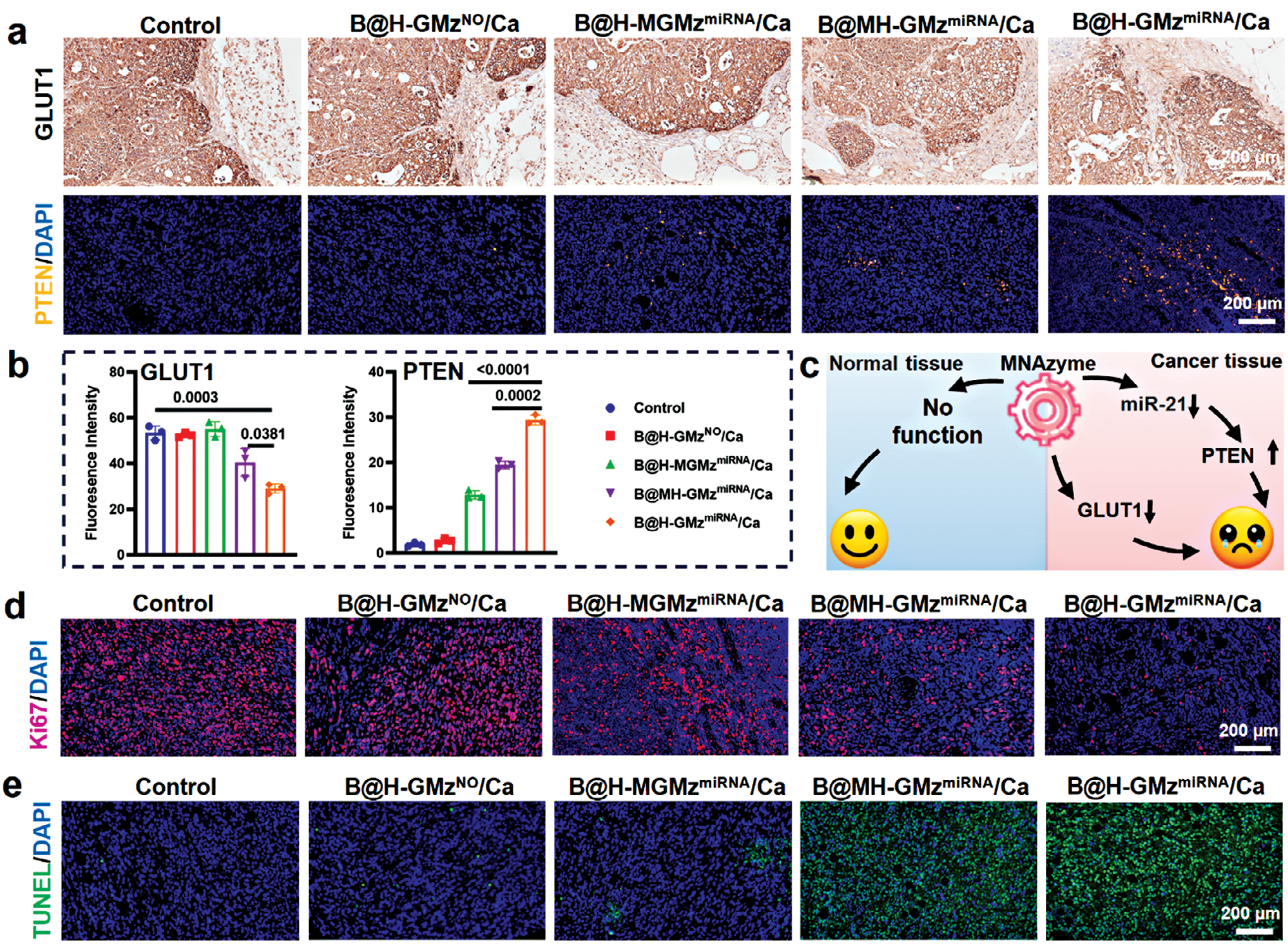

Figure 7. Analysis of protein expression levels induced by MNF nanomaterials in mice. a) The expression of GLUT1 and PTEN across different tissue slice groups. b) Quantitative analysis of GLUT1 and PTEN expression levels using ImageJ. c) The tumor targeting mechanism of smart MNF nanomaterials. d) Ki-67 and e) TUNEL, along with DAPI-stained tumor slices imaged by DLSM.

were monitored during the treatment period, with no significant variances found between the treated and control groups, suggesting no detrimental impact on overall health (Figure 6d).

Finally, we assessed the expression of GLUT1 in tumor slices; significant reduction in red fluorescence (GLUT1) was evident in tumors treated with B@MH-GMz^{miRNA}/Ca and B@H-GMz^{miRNA}/Ca, while strong red fluorescence was clearly observable in other groups. This phenomenon compellingly demonstrates that B@H-GMz^{miRNA}/Ca MNFs can effectively reduce the expression of GLUT1 in vivo (**Figure** 7a,b). Subsequently, further investigation was conducted into the silencing effect of miRNA-21 mediated by the MNAzyme system. Silencing miRNA-21 can mediate the upregulation of PTEN, thereby inhibiting tumor growth. The results in Figure 7a,b reveal that for the formulation groups capable of capturing miRNA-21, namely B@H-MGMz^{miRNA}/Ca, B@MH-GMz^{miRNA}/Ca, and B@H-GMz^{miRNA}/Ca, there was a varying increase in PTEN levels, with the B@H-GMz^{miRNA}/Ca group exhibiting the highest level of PTEN protein expression. These outcomes demonstrate the MNAzyme system's excellent capability for miRNA-21 recognition and silencing in vivo, effectively reducing GLUT1 expression in cancerous tissues and upregulating PTEN expression levels (Figure 7c). Moreover, in tumor slices from the B@MH-GMz^{miRNA}/Ca and B@H-GMz^{miRNA}/Ca groups, negligible Ki-67 (Figure 7d) signal and a significant TUNEL signal (Figure 7e) were observed, indicating a higher number of apoptotic cells and fewer proliferating cells.

3. Conclusion

Compared to metal-organic frameworks, the main advantage of constructing Metal-Nucleic Acid Frameworks (MNFs) using MNAzyme ligands lies in effectively harnessing the multifunctionality of MNAzyme sequences. These sequences can identify disease tissues and provide corresponding therapeutic functions. Integration of aptamer sequences further imparts targeting capabilities to the MNFs. Therefore, when employing MNF materials for drug delivery, the construction of the carrier is streamlined, circumventing the inclusion of non-therapeutic elements, while leveraging the multifunctional nature of the MNAzyme sequences. MNFs, as emerging functional carriers, offer significant research potential in terms of properties and synthesis methods compared to extensively studied MOFs.

In this work, we designed a multifunctional MNAzyme sequence capable of biomarker recognition and targeting Her-2 overexpressed cancer cells. We explored the mechanism of this sequence binding with calcium ions, highlighting the critical importance of DNA length in facilitating the fabrication of Metal-Nucleic Acid Frameworks at room temperature. Considering the functionality of DNA sequences, a longer sequence allows for more flexible and extensive design possibilities. As demonstrated in our study, integrating the Her-2 aptamer targeting sequence into a calcium-ion-dependent MNAzyme sequence, recognizing the cancer biomarker miRNA-21 for dual-gene regulation of GLUT1 mRNA and miRNA-21, enabled precise and intensified energy exhaustion therapy. Thus, our work ingeniously combines MNAzyme and MNF, bringing new opportunities to both research fields.

Supporting Information

Supporting Information is available from the Wiley Online Library or from the author.

Acknowledgements

X.M., J.Y., and G.Z. contributed equally. This work was supported by the National Natural Science Foundation of China (Grant No. 82372145 (H.Z.)). It was also supported by the Research Fellow (Grant No. 353146 (H.Z.)), Project (Grant No. 347897 (H.Z.)), Solution for Health Profile (Grant No. 336355 (H.Z.)), and InFLAMES Flagship (Grant No. 337531 (H.Z.)) grants from the Academy of Finland, Finland, The China Food and Health International Pilot Project (H.Z.) funded by the Finnish Ministry of Education and Culture, The Leading Talents in Scientific and Technological Innovation from Zhejiang Provincial Ten Thousand Talents Plan (Grant No. 2019R52021 (X.S.)), The Key Research and Development Program of Zhejiang Province (Grant No. 2021C03120 (X.S.)). The Key Research and Development Program of Wenzhou (Grant No: ZY2021003 (X.S.)), the National Natural Science Foundation (Grant Nos. 82272172 (W.S.), 81972261 (W.S.), the Medical Health Science and Technology key Project of Zhejiang Provincial and Ministry Health Commission (Grant No. WKJ-ZJ-2322 (W.S.)), the Wenzhou Basic Public Welfare Research Project (Grant No. 2021Y0056 (G.Z.)).

Conflict of Interest

The authors declare no conflict of interest.

Data Availability Statement

The data that support the findings of this study are available from the corresponding author upon reasonable request.

Keywords

Ca^{2+} homeostasis disruption, cancer targeting, energy exhaustion, metal-nucleic acid frameworks, MNAzyme

Received: April 24, 2024
Revised: May 22, 2024
Published online:

---

[1] J. Yan, M. Ran, X. Shen, H. Zhang, *Adv. Mater.* **2023**, *35*, 2300374.
[2] S. W. Santoro, G. F. Joyce, *Proc. Natl. Acad. Sci. U.S.A.* **1997**, *94*, 4262.
[3] Y. Jiao, Y. Shang, N. Li, B. Ding, *iScience* **2022**, *25*, 104018.
[4] W. Zhou, J. Ding, J. Liu, *Theranostics* **2017**, *7*, 1010.
[5] W. Hou, Q. Ni, J. Wo, M. Li, K. Liu, L. Chen, Z. Hu, R. Liu, M. Hu, *Antiviral Res.* **2006**, *72*, 190.
[6] N. Verma, S. K. Tripathi, I. Chaudhury, H. R. Das, R. H. Das, *Shock* **2010**, *33*, 493.
[7] H. Cai, F. S. Santiago, L. Prado-Lourenco, B. Wang, M. Patrikakis, M. P. Davenport, G. J. Maghzal, R. Stocker, C. R. Parish, B. H. Chong, G. J. Lieschke, T.-W. Wong, C. N. Chesterman, D. J. Francis, F. J. Moloney, R. S. C. Barnetson, G. M. Halliday, L. M. Khachigian, *Sci. Transl. Med.* **2012**, *4*, 139ra82.
[8] W. Zhou, Q. Chen, P.-J. J. Huang, J. Ding, J. Liu, *Anal. Chem.* **2015**, *87*, 4001.
[9] E. Mokany, S. M. Bone, P. E. Young, T. B. Doan, A. V. Todd, *J. Am. Chem. Soc.* **2010**, *132*, 1051.
[10] S. Safdar, J. Lammertyn, D. Spasic, *Trends Biotechnol.* **2020**, *38*, 1343.
[11] D. Zhu, Y. Wei, T. Sun, C. Zhang, L. Ang, S. Su, X. Mao, Q. Li, C. Fan, X. Zuo, J. Chao, L. Wang, *Anal. Chem.* **2021**, *93*, 2226.
[12] N. Wang, L. Song, Y. Qiu, H. Xing, J. Li, *Sensor. Actuat. B-Chem.* **2019**, *286*, 250.
[13] X. Yin, B. Chen, M. He, B. Hu, *Anal. Chem.* **2021**, *93*, 4952.
[14] M. A. Abdou Mohamed, H. N. Kozlowski, J. Kim, K. Zagorovsky, M. Kantor, J. J. Feld, S. Mubareka, T. Mazzulli, W. C. W. Chan, *ACS Nano* **2021**, *15*, 9379.
[15] H. N. Kozlowski, M. A. Abdou Mohamed, J. Kim, N. G. Bell, K. Zagorovsky, S. Mubareka, W. C. W. Chan, *Small Struct.* **2021**, *2*, 2100034.
[16] W. Zhou, Y. Zhang, J. Ding, J. Liu, *ACS Sens.* **2016**, *1*, 600.
[17] J. Yan, X. Ma, D. Liang, M. Ran, D. Zheng, X. Chen, S. Zhou, W. Sun, X. Shen, H. Zhang, *Nat. Commun.* **2023**, *14*, 6905.
[18] Z. Wang, J. Yang, G. Qin, C. Zhao, J. Ren, X. Qu, *Angew. Chem., Int. Ed.* **2022**, *61*, e202204291.
[19] S. Schubert, D. C. Gül, H. P. Grunert, H. Zeichhardt, V. A. Erdmann, J. Kurreck, *Nucleic Acids Res.* **2003**, *31*, 5982;
[20] H. Fan, X. Zhang, Y. Lu, *Sci. China: Chem.* **2017**, *60*, 591.
[21] Y. Li, R. Bhindi, Z. J. Deng, S. W. Morton, P. T. Hammond, L. M. Khachigian, *Int J Cardiol* **2013**, *168*, 3659.
[22] X. Ke, Y.-C. Yang, S.-L. Hong, *Med Oncol* **2011**, *28*, 326.
[23] H. Zhang, J. Guo, Y. Wang, L. Shang, R. Chai, Y. Zhao, *Adv. Funct. Mater.* **2022**, *32*, 2203829.
[24] Z. Xing, S. Gao, Y. Duan, H. Han, L. Li, Y. Yang, Q. Li, *Int. J. Nanomed.* **2015**, *10*, 5715.
[25] S. Li, M. Meng Lin, M. S. Toprak, D. K. Kim, M. Muhammed, *Nano Rev* **2010**, *1*, 5214.
[26] K. Yehl, J. P. Joshi, B. L. Greene, R. B. Dyer, R. Nahta, K. Salaita, *ACS Nano* **2012**, *6*, 9150.
[27] J. Victor, G. Steger, D. Riesner, *Eur. Biophys. J.* **2018**, *47*, 333.
[28] S. Wu, K. Zhang, Y. Liang, Y. Wei, J. An, Y. Wang, J. Yang, H. Zhang, Z. Zhang, J. Liu, J. Shi, *Adv. Sci.* **2022**, *9*, 2103534.
[29] Y. Li, P. Zhao, T. Gong, H. Wang, X. Jiang, H. Cheng, Y. Liu, Y. Wu, W. Bu, *Angew. Chem., Int. Ed.* **2020**, *59*, 22537.
[30] Y. Liu, Z. Liu, R. Liu, K. Wang, H. Shi, J. Huang, *Analyst* **2021**, *146*, 3391.
[31] M. Li, C. Wang, Z. Di, H. Li, J. Zhang, W. Xue, M. Zhao, K. Zhang, Y. Zhao, L. Li, *Angew. Chem., Int. Ed.* **2019**, *58*, 1350.
[32] B. Liu, F. Hu, J. Zhang, C. Wang, L. Li, *Angew. Chem., Int. Ed.* **2019**, *58*, 8804.
[33] Y. Yang, B. Liu, Y. Liu, J. Chen, Y. Sun, X. Pan, J. Xu, S. Xu, Z. Liu, W. Tan, *Nano Lett.* **2022**, *22*, 2826.
[34] A. J. Senesi, D. J. Eichelsdoerfer, K. A. Brown, B. Lee, E. Auyeung, C. H. J. Choi, R. J. Macfarlane, K. L. Young, C. A. Mirkin, *Adv. Mater.* **2014**, *26*, 7235.

[35] S. J. Maassen, M. V. de Ruiter, S. Lindhoud, J. J. L. M. Cornelissen, *Chemistry* **2018**, *24*, 7456.
[36] S. Xiao, H. Liang, D. J. Wales, *J. Phys. Chem. Lett.* **2019**, *10*, 4829.
[37] Y. Chen, Y. Song, Z. He, Z. Wang, W. Liu, F. Wang, X. Zhang, X. Zhou, *Nano Res.* **2016**, *9*, 3084.
[38] H. Lee, D. H. M. Dam, J. W. Ha, J. Yue, T. W. Odom, *ACS Nano* **2015**, *9*, 9859.
[39] G. Mahlknecht, R. Maron, M. Mancini, B. Schechter, M. Sela, Y. Yarden, *Proc. Natl. Acad. Sci. USA* **2013**, *110*, 8170.
[40] X. Liu, K. Olszewski, Y. Zhang, E. W. Lim, J. Shi, X. Zhang, J. Zhang, H. Lee, P. Koppula, G. Lei, L. Zhuang, M. J. You, B. Fang, W. Li, C. M. Metallo, M. V. Poyurovsky, B. Gan, *Nat. Cell Biol.* **2020**, *22*, 476.
[41] Y. Xiao, Z. Li, A. Bianco, B. Ma, *Adv. Funct. Mater.* **2022**, *33*, 202209291.
[42] J. Yao, H. Peng, Y. Qiu, S. Li, X. Xu, A. Wu, F. Yang, *J Mater Chem B* **2022**, *10*, 1508.
[43] Y. Li, S. Zhou, H. Song, T. Yu, X. Zheng, Q. Chu, *Biomaterials* **2021**, *277*, 121080.
[44] A. Peracchi, *J. Biol. Chem.* **2000**, *275*, 11693.
[45] W. J. Moon, Y. Yang, J. Liu, *ChemBioChem* **2021**, *22*, 779.
[46] H. Zhou, H. Liu, M. Jiang, S. Zhang, J. Chen, X. Fan, *Cell Transplant.* **2019**, *28*, 306.
[47] B. G. Zhang, J. F. Li, B. Q. Yu, Z. G. Zhu, B. Y. Liu, M. Yan, *Oncol Rep* **2012**, *27*, 1019.
[48] X. Liu, J. M. Abraham, Y. Cheng, Z. Wang, Z. Wang, G. Zhang, H. Ashktorab, D. T. Smoot, R. N. Cole, T. N. Boronina, L. R. DeVine, C. C. Talbot, Z. Liu, S. J. Meltzer, *Molecular Therapy – Nucleic Acids* **2018**, *13*, 312.
[49] B. R. Wolfe, N. J. Porubsky, J. N. Zadeh, R. M. Dirks, N. A. Pierce, *J. Am. Chem. Soc.* **2017**, *139*, 3134.